Volume 24, No 2 | International Journal of Radiation Research, April 2026

Synthesizing computed tomography images from magnetic resonance images for cervical cancer radiotherapy treatment planning

D. Jiang[#], Y. Tian[#], X. Peng[#], L. Yang[*], H. Liu[*]

Radiotherapy Center, Hubei Key Laboratory of Tumor Biological Behaviors, Hubei Cancer Clinical Study Center, Zhongnan Hospital of Wuhan University, Wuhan, China

► ***Original article***

Corresponding author:
Lan Yang, M.D.;
Hui Liu, M.D.;
E-mail:
yangl_zn@163.com,
hbzknyy@163.com

Received: December 2024
Final revised: September 2025
Accepted: October 2025

Int. J. Radiat. Res., April 2026; 24(2): 527-533

DOI: 10.61186/ijrr.24.2.33

Keywords: *Magnetic resonance imaging; radiotherapy planning, cervical cancer, Generative adversarial network, synthetic computed tomography.*

#These authors contributed equally to this work.

ABSTRACT

Background: This study aimed to explore using computed tomography (CT) images synthesized from magnetic resonance (MR) images by the 2.5D semi-supervised generative adversarial nets (SSGAN) framework to enhance the precision of intensity-modulated radiotherapy (IMRT) planning in patients with cervical cancer. ***Materials and Methods:*** A comprehensive pelvic MR-CT dataset, encompassing T1-weighted MR and CT volumes from 174 subjects, was utilized. This dataset was divided into training (n = 150) and test (n = 24) sets for model development and assessment. The Hounsfield Unit (HU) discrepancy and dosimetric accuracy of synthetic CT (sCT) images generated by 2.5D SSGAN were evaluated against actual CT images for cervical cancer IMRT planning. ***Results:*** The mean gamma analyses values for 2D criteria of 1 mm/1%, 2 mm/2%, and 3 mm/3% in these planes were 92.18% ± 4.64%, 98.13% ± 3.05%, and 99.23% ± 1.52%, respectively. Absolute dose deviations averaged 0.51% ± 0.18% within the regions of interest (ROIs). ***Conclusion:*** SSGAN accurately synthesized CT images from MR images, maintaining high dosimetric accuracy essential for cervical cancer IMRT planning.

INTRODUCTION

Radiation therapy, also known as radiotherapy, stands as a pillar in the treatment of tumors. Historically, simulated computed tomography (CT) imaging has been the primary source of image data for planning radiotherapy in oncology. Simulated CT images accurately represent the patient's anatomical structure, with CT values that can be translated into electron density information essential for radiation dose calculation. However, CT images fall short in soft-tissue contrast, making it challenging to delineate tumor and soft tissue boundaries accurately. Additionally, CT exposes patients to radiation during scanning.

In contrast, magnetic resonance imaging (MRI) excels in soft tissue contrast, depicting tumors and soft tissues with remarkable clarity, and without exposing the patients to any radiation during acquisition [1, 2]. Consequently, it is common in clinical practice to align patient MR images and data with the simulated localized CT images, and then outline tumor and normal tissues on the latter to create an oncology radiation treatment plan. However, this process complicates radiotherapy and introduces alignment errors as the MR and CT images were scanned in different positions, decreasing the tumor localization accuracy.

Consequently, MRI-only guided radiotherapy technology has emerged as a focal point of research [3-5]. This technique utilizes MR images to replace traditional simulated CT images for localization, planning, dose calculation, and image-guided pose correction. MRI-guided radiotherapy simplifies the process, accurately outlines tumor and normal tissues, and avoids errors associated with CT and MR image alignment. The primary challenge lies in that MRI intensity values are not directly correlated with electron density information, hindering dose calculation. Since conventional radiotherapy planning necessitates CT images for dose calculation, current solutions synthesize corresponding synthetic CT (sCT) images from MR images [6-8].

Traditional MR-to-sCT synthesis algorithms can be broadly categorized into tissue segmentation-based and atlas-based methods. Our study on a pre-segmentation method revealed that aspects like mean value and organ assignments, used in cervical cancer

[DOI: 10.61186/ijrr.24.2.33]

radiotherapy planning, were inaccurate [11]. Atlas-based methods generate reliable sCT data from conventional MR data, but current alignment algorithms are time-consuming and need refinement, especially for data with significant anatomical or pathological differences.

Recent advances in deep learning have prompted scholars to employ supervised learning through convolutional neural networks (CNNs) to synthesize sCT images. These CNNs use aligned MR/CT data pairs by pairing voxels for training. Through supervised learning, CNNs predict the HU value for each voxel in the MR image more accurately. Han *et al*. [10] achieved superior results with a two-dimensional deep CNN model for synthesizing sCT from brain MR data compared to traditional algorithms. However, CNNs are limited by alignment errors in training data pairs, resulting in blurred sCT images. To address this, Nie *et al*. [11] introduced generative adversarial networks (GANs) to enhance the sCT image quality. GANs consist of a generator that synthesizes sCT images and a discriminator that compares them to real CT images, prompting the generator to produce realistic sCT images. Although GANs can generate realistic sCT images, alignment errors in data pairs remain a challenge.

Zhu *et al*. [12] proposed the cycleGAN model for image domain translation, synthesizing images from different domains. CycleGANs require only unaligned data pairs for training, bypassing the issues of data pair acquisition and alignment errors. Jelmer *et al*. [13] used a two-dimensional (2D) cycleGAN model to synthesize brain sCT images from corresponding MR images, yielding results comparable to those from aligned data pairs. Liu *et al*. [14] employed a cycleGAN model to synthesize sCT images from corresponding pelvic MR images, achieving excellent pelvic data alignment results.

While these studies demonstrated cycleGAN's effectiveness in synthesizing sCT images, they were limited to 2D models [12, 13]. Studies have shown that 2.5D networks provide richer semantic information and improve sCT image accuracy compared to 2D networks [14-16].

The novelty of this study lies in the development of a 2.5D semi-supervised generative adversarial network (SSGAN) framework tailored for synthesizing sCT images from pelvic MR scans for cervical cancer radiotherapy. Unlike conventional methods (e.g., cycleGAN or atlas-based approaches), our model integrates three key innovations: (1) a transformer-enhanced generator to capture global anatomical relationships and mitigate alignment errors inherent to unpaired MR-CT training data; (2) a contrastive learning loss that enforces semantic consistency between sCT and real CT patches, improving edge sharpness in critical regions such as bone and soft-tissue interfaces; (3) a 2.5D volumetric architecture that leverages multi-slice contextual information to enhance spatial accuracy while maintaining computational efficiency. These advancements collectively address the limitations of existing 2D models (e.g., blurred sCT outputs) and atlas-based techniques (e.g., registration failures in pathological anatomies).

MATERIALS AND METHODS

Study population and data acquisition

The study population included 174 patients, aged 43–83 years, diagnosed with cervical cancer at Zhongnan Hospital of Wuhan University (ZNWH) between January and November 2022.

A Philips 16-slice large-aperture analog positioning scanner was used to perform CT scans, and the parameters were set to 280 mAs,140 kV and 3 mm slice thickness. A GE Discovery MR750 3.0T MRI scanner was used to get the pelvic MRI. The MRI scanning parameters were as follows: TR of 3,200 ms, TE of 85 ms, slice thickness of 3 mm, slice interval of 0.5 mm, and a field of view of 16×16 cm.

All patients were scanned during radiotherapy on a flat tabletop using a coil setup that did not alter their outline.

The data collected at the hospital comprised diagnostic MRI and positional CT images. Notably, significant deformation rendered the MR and CT images unpairable. Conversely, the public datasets contained localized MR and CT data that had been aligned to account for deformation, making them paired data.

Image preprocessing and registration

Body on the CT and MR images were generated using a treatment planning system (TPS) (Shanghai, China, United Imaging Healthcare Co., Ltd.). Voxel intensities outside the external contours were assigned values of –1,024 for CT images and 0 for MR images. CT image intensities were linearly mapped from the CT range of (–1,024 to 1,500) to the MRI range of (–1 to 1). After clipping MR image intensities over the 95th percentile, the remaining intensities were linearly mapped to the (–1 to 1) range. NiftyReg, an open-source program, was used to conduct deformable registration on the CT and MR images [2].

The pelvic MR-CT dataset comprised CT and T1-weighted MR from all 174 subjects. It was randomly divided into testing (n = 24) and training (n = 150), enabling accurate performance evaluation and assessment of the developed models or algorithms.

Network architecture design

The proposed 2.5D SSGAN framework consisted of two discriminators (D_{MR} and D_{CT}) and two generators (G_{MR} and G_{CT}) [3]. G_{CT} performed MR to CT mapping, while G_{MR} performed CT to MR mapping. D_{CT} and D_{MR} were employed to distinguish between real and synthetic images. The overall structure of 2.5D

[DOI: 10.61186/ijrr.24.2.33]

SSGAN is depicted in figure 1.

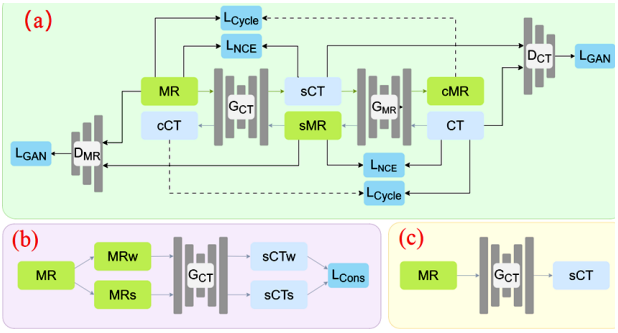

Figure 1. 2.5D SSGAN framework. **(a)** MR-to-CT training, **(b)** CT -to-MR training, **(c)** Synthetic CT inference. Abbreviations: GCT (MR-to-CT generator), DCT (CT discriminator), CL (Contrastive Learning).

The loss function of 2.5D SSGAN for unpaired data included cycle loss, adversarial loss, and contrastive learning (CL) loss. Paired data incorporated supervised loss in addition to unsupervised losses such as mutual information, L1, VGG, structural similarity index measure (SSIM), and gradient difference losses. A 2.5D image, representing two consecutive adjacent layers within a specific volume, was used as the input. In order to minimize the loss, function the Adam optimization method was employed. The He, normal initialization method initialized the 2.5D SSGAN framework.

Generator with transformer module

The generator in the 2.5D SSGAN framework used the Transformer module. Unlike the convolution module, this module offers the advantage of extracting deep features while facilitating attention to global feature connections. Due to its enhanced effectiveness, the Transformer module was specifically applied to the last encoder layer of the generator.

Discriminator with spectral normalization

This was accomplished by adding spectral normalization to the discriminator in simple cycleGAN, which allowed the discriminator networks in 2.5D SSGAN to have the same architecture. By applying regularity restrictions to the spectral norm of each layer's parameter matrix, spectral normalization increases the network's resistance to input disruptions.

Loss function formulation

The study employed a mixed loss function to optimize the generator and discriminator networks for training unsupervised data, which included adversarial, cycle consistency, and CL losses.

The adversarial loss function (L_{adv}) optimized the generator (G_{CT}) and its discriminator (D_{CT}) (equation 1):

$$L_{adv}(G_{CT}, D_{CT}) = D_{CT}(G_{CT}(I_{MR})) + (1 - D_{CT}(I_{CT})) \quad (1)$$

Here, I_{CT} and I_{MR} represent unpaired input CT and MR images, respectively. During training, G_{CT} generates an sCT image ($G_{CT}(I_{MR})$) that should resemble a real CT image (I_{CT}), while D_{CT} aims to distinguish the sCT image from a real image.

The cycle-consistent loss function (L_{cycle}) optimizes G_{CT} and G_{MR} by ensuring that the reconstructed images [G_{CT} (G_{MR} (I_{CT})] and G_{MR} [G_{CT} (I_{MR})] are similar to their respective input images (equation 2):

$$L_{cycle}(G_{CT}, G_{MR}) = \|G_{CT}(G_{MR}(I_{CT})) - I_{CT}\| + \|G_{MR}(G_{CT}(I_{MR})) - I_{MR}\| \quad (2)$$

Evaluation metrics

Mean absolute error (MAE): This study used the MAE to measure the difference in Hounsfield units (HUs) between sCT and CT images, calculated as the average absolute difference between corresponding pixel intensities (equation 3):

$$\mathrm{MAE} = \frac{1}{N}\sum_{i=1}^{N}|CT_i - sCT_i| \quad (3)$$

Peak signal-to-noise ratio (PSNR): The PSNR was employed as an objective measure of image distortion or noise level. It quantifies the ratio of the maximum possible signal power to the mean squared error (MSE) of the image (equation 4):

$$\mathrm{PSNR} = 10 * log_{10}\left(\frac{MAX_I^2}{MSE}\right) \quad (4)$$

SSIM: The SSIM evaluated the similarity between images in brightness, structure, and contrast. It is calculated based on the mean, standard deviation, and covariance of pixel intensities (equation 5):

$$\mathrm{SSIM} = \frac{(2\mu_x\mu_y + C_1)(2\sigma_{xy} + C_2)}{(\mu_x^2 + \mu_y^2 + C_1)(\sigma_x^2 + \sigma_y^2 + C_2)} \quad (5)$$

Dosimetric analysis

For the dosimetric analysis study, we selected 24 patients with cervical cancer who underwent IMRT between January 2021 and July 2022. The inclusion criteria were: (1) stage IB-IIB disease, (2) biopsy-confirmed squamous cell carcinoma, and (3) had undergone postoperative pelvic radiation therapy. Individuals who had concurrent integrated boost therapy and had high-risk pelvic lymph nodes were not included. This cohort's median age was 61 years, while its mean age was 56.3 years (range, 42–65).

A helical CT scanner (Sensation Cardiac 64x, Siemens, Munich, Germany) with a slice thickness of 3 mm was used to simulate CT scans for each patient. The scans covered the area from the L1 vertebra to 5 cm below the ischial tuberosities.

We used clinical pelvic treatment plans to analyze the dosimetric accuracy when when planning with sCT images The primary tumor target was prescribed a dose of 5,0 Gy. A 6-MV X-rays IMRT plan with nine beams was designed for each patient using uRT-linac 506C.

The planned dose distribution was recalculated in

[DOI: 10.61186/ijrr.24.2.33]

a quality assurance mode using the sCT images instead of the genuine CT images, with identical beam parameters. The dosage matrices covered the main regions of interest (ROIs), such as the femoral head and pelvis, with a resolution of 3×3×3 mm. The dose matrices were compared using a global 2D gamma analysis.

RESULTS

Image comparison

The results of the test group are presented in figure 2. In the majority of the locations, the sCT images produced by the models showed satisfactory quality; in the first sample, there was a clear contrast between the surrounding soft tissues and the bone. On the sCT images, however, some differences were seen in specific bone areas, as shown in figures 2b and 2c. As seen in figures 2e and 2f, the bone edge sharpened when the CL loss was included in the model. Notably, our suggested 2.5D SSGAN with CL loss model (figure 2f) outperformed the other models in terms of accuracy in capturing the values and structure of the bone.

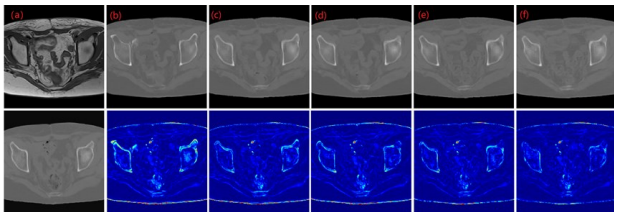

Figure 2. Synthetic CT (sCT) images generated by different models. **(a)** Ground truth (GT) and input MR image. **(b)** CycleGAN. **(c)** 2.5D CycleGAN. **(d)** 2.5D RTGAN. **(e)** 2.5D RTGAN with CL loss. **(f)** Proposed 2.5D SSGAN with CL loss.

To evaluate the precision of sCT images generated for treatment planning, we calculated SSIM, MAE, and PSNR across the entire outer contour of each patient in the test set for every model (table 1). Our findings demonstrated that the sCT outcomes were enhanced by the transformer module or by incorporating CL loss into the model. Combining both into the cycleGAN model improved the sCT images' performance even more.

Table 1. Evaluating MAE, SSIM, and PSNR for sCT generated by various methods across the entire pelvic region.

Method	MAE ↓	PSNR ↑	SSIM ↑
CycleGAN	52.858	23.153	0.976
2.5D CycleGAN	49.801	24.926	0.983
2.5D RTGAN	48.127	25.578	0.984
2.5D RTGAN (w/ CL loss)	44.681	25.962	0.983
2.5D SSGAN (w/ CL loss)	43.837	26.077	0.984

Note: RTGAN: Restransformer generative adversarial nets; SSGAN: Semi-supervised generative adversarial nets; CL: Contrastive learning.

Dose comparison

The differences in dose distribution are shown in figures 3 and 4. Figure 3 shows that dosimetric difference is almost absent. Figure 4 shows that the area with significant dose deviation is at the edge of the skin. The dose-volume histogram (DVH) values computed between the SCT and real CT images was shown in Figure 5. To quantitatively evaluate the dosimetric accuracy, the absolute dose deviations for key regions of interest (ROIs) were calculated and are summarized in table 2. For the primary target volume (PTV), all dose parameters including Dmax, Dmean, D95%, D5%, and D2% showed mean deviations of less than 0.4%, with the largest deviation observed in D5% (0.38% ± 0.21%). Among the organs at risk (OARs), the largest mean dose deviation was observed for the Dmean of the rectum (0.79% ± 0.12%).

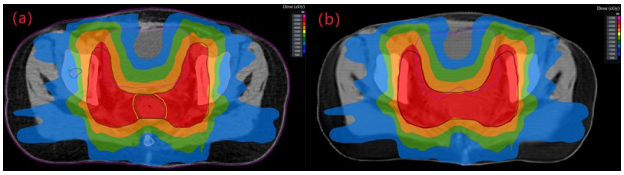

Figure 3. shows the difference in dose between raw CT and sCT for one example patient. The figure shows the dose distribution of 50Gy, 40Gy, 30Gy, and 20Gy for the original CT, while the figure b shows results for sCT.

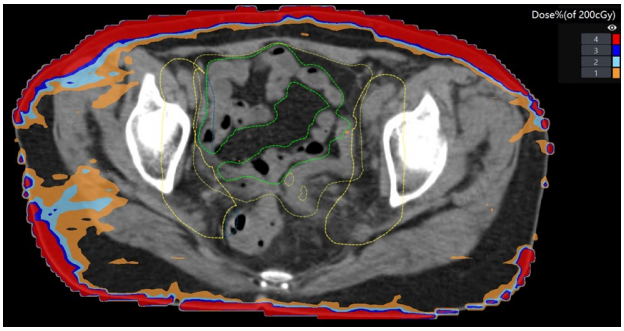

Figure 4. shows the difference in dosage between two plans. The dose deviation ranges from 1% to 4% with different colors for one example patient.

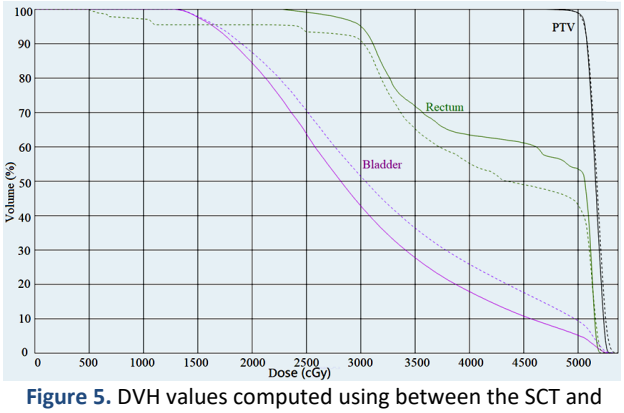

Figure 5. DVH values computed using between the SCT and real CT images for one example patient.

Gamma analyses in the coronal, sagittal, and transverse dose planes showed mean 2D 1 mm/1%, 2 mm/2%, and 3 mm/3% values of 92.18% ± 4.64%, 98.13% ± 3.05%, and 99.23% ± 1.52%, respectively.

Mean 2D gamma passing rates (± standard deviation) were 92.18% ± 4.64% (1 mm/1%), 98.13% ± 3.05% (2 mm/2%), and 99.23% ± 1.52%

[DOI: 10.61186/ijrr.24.2.33]

(3 mm/3%), respectively.

Table 2. Absolute dose deviations for different regions of interest.

Organ	Parameter	Mean	Standard deviation
PTV	Dmax	0.19%	0.12%
	Dmean	0.35%	0.31%
	D95%	0.15%	0.11%
	D5%	0.38%	0.21%
	D2%	0.19%	0.16%
Bladder	Dmax	0.27%	0.17%
	Dmean	0.47%	0.22%
Rectum	Dmax	0.45%	0.27%
	Dmean	0.79%	0.12%
Small bowel	Dmax	0.18%	0.14%
	Dmean	0.60%	0.33%
Femoral heads	Dmax	0.43%	0.37%
	Dmean	0.25%	0.12%
Pelvis	Dmax	0.27%	0.08%
	Dmean	0.32%	0.13%

DISCUSSION

The present study explored the feasibility of synthesizing pelvic CT images from MR scans using a 2.5D SSGAN framework for MRI-only radiotherapy planning in cervical cancer. The study indicates robust performance in preserving anatomical details and HU accuracy, particularly at the bone-soft-tissue interface.

Our dosimetric evaluation revealed minimal deviations, with absolute dose differences for all regions of interest (ROIs) averaging less than 0.8%. These dose differences are well within the clinically acceptable tolerance of ±2.0% often considered significant for radiotherapy [17]. This high level of accuracy is consistent with findings from other studies utilizing deep learning for sCT generation in the pelvis. For instance, Hsu *et al.* [18] reported similarly low DVH dose deviations of less than 0.8% in their study on MRI-guided adaptive radiotherapy for prostate cancer, with the largest discrepancy also observed in the rectum (D2cc). Notably, both studies found minimal deviations in more stable bony structures like the femoral heads and pelvis, reinforcing the reliability of sCT for dose calculation in these areas. The observed variations in hollow organs like the rectum and bowel are a common challenge, as highlighted by Kang *et al.* [19], who using a cycle-consistent GAN, also found that dose deviations in the intestine were generally larger than those in bone. This consensus across studies underscores that while sCT generation is highly accurate overall, inter-fractional anatomical changes in soft tissues remain a primary source of residual dosimetric uncertainty.

Arabi *et al.* [20] compared six sCT image generation algorithms and reported mean MAEs of 32.7±7.9 to 52.1±11.1 HU. The lowest MAE was achieved using a deep convolutional neural network (DCNN) algorithm. Gholamiankhah *et al.* [21] reported MAEs of 114.1±27.5 and 161.3±38.1 HU when using ResNet and GAN models, respectively, for brain sCT image generation, highlighting ResNet's superiority in preserving structural accuracy due to its residual connections and high-resolution processing. Liu *et al.* generated sCT images using DCNN and reported a mean MAE of 58.98±18.64 HU, which could be due to the specific algorithm employed. Overall, our study's mean MAE was comparable to state-of-the-art techniques. This is particularly noteworthy given that the pelvis and abdomen are among the most challenging regions for sCT synthesis due to respiratory motion and significant inter- and intra-fraction organ movement [22]. The accuracy achieved in such an environment demonstrates the potential of our 2.5D SSGAN framework. Our gamma analysis outcomes were similar to those reported in pelvis studies by Koivula *et al.* [23], Liu *et al.* [14], and Maspero *et al.* [24]. In separate retrospective studies of ten prostate cancer patients each, one investigation [14] reported an average 3D 2 mm/2% gamma pass rate of 98.4%, while Koivula *et al.* [23], employing a segmentation-based dual model HU conversion technique, found average 3D pass rates of 95.0%, 98.6%, and 99.6% for the 1 mm/1%, 2 mm/2%, and 3 mm/3% criteria, respectively. Our results were slightly inferior, possibly due to differences in methods, datasets, and gamma analysis techniques.

The choice of AI model architecture significantly influences the quality and accuracy of the generated sCT images. While our study employed a transformer-enhanced GAN, other architectures like U-Net [25] and various GAN derivatives [26, 27] have been successfully applied to medical image synthesis tasks, each with its strengths. For example, U-Net is renowned for its precise segmentation capabilities in tasks such as metal artifact reduction [25] or aorta segmentation [26], which relies on its powerful encoder-decoder structure with skip connections. A comprehensive comparative study by Lapaeva *et al.* [28] on GAN architectures for abdominal sCT generation further emphasizes that no single model universally outperforms all others, and the optimal architecture may be task-specific. Our 2.5D SSGAN framework, which integrates transformer modules and contrastive learning, represents one effective approach tailored to handle the specific challenges of unpaired pelvic MR-CT synthesis, demonstrating performance on par with or superior to other contemporary methods.

Small changes in the PTV of the CT and original MR images were observed in the pelvis and femoral head, while larger changes were noted in the bowel. This was primarily due to substantial intestinal alterations between the initial MRI and CT images, whereas pelvic and femoral head abnormalities were

[DOI: 10.61186/ijrr.24.2.33]

relatively minor. Hsu *et al*. [18] reported similarly low DVH dose deviations of less than 0.8% in their study on MRI-guided adaptive radiotherapy for prostate cancer, with the largest discrepancy also observed in the rectum (D2cc). Kang *et al*. [19] showed the significant DVH difference between dCT and -sCTU-net, which is largest in the PTV. The differences were observed between bladder and rectum DVH measurements, primarily due to geometric discrepancies caused by non-concurrent acquisition of MR and CT images, resulting in natural variations in organ filling status. Additionally, the MR images used in our study were diagnostic data from the imaging department, with significant differences in body position data due to the absence of irradiation fixation devices. Furthermore, internal differences were minor compared to significant shape contour dose biases, indicating that variations in patient positioning between sCT and CT were the primary cause of greater dose discrepancies for some patients, rather than inaccurate HU assignment. However, these differences were small and fell within the ±2.0% threshold often considered clinically significant [17].

An important consideration in MR-only radiation therapy is the clinically meaningful level of dose variations. Dosimetric and geometric uncertainties should be within 3% and 2-4 mm, respectively, throughout the treatment pathway [29]. For most patients, this suggests that the sCT images are dosimetrically accurate enough for clinical use. However, given the greater dose variation observed in one patient, patient-specific quality assurance of the sCT dose calculation accuracy is needed [30].

Limitations and future directions

This study has several limitations. First, the model was trained and validated on a single-center dataset (n=174), raising concerns about generalizability across different institutions, MR scanner protocols, and patient populations. Second, while the SSGAN framework reduces alignment errors, residual dosimetric discrepancies in bowel and bladder (attributed to non-concurrent MR/CT acquisition) necessitate standardized same-day imaging protocols. Third, the focus was exclusively on cervical cancer; validation for other pelvic malignancies (e.g., prostate or rectal cancer) is required. Finally, the computational complexity of the 2.5D architecture may hinder real-time clinical integration, warranting optimization for faster inference.

***Acknowledgements*:** The authors thank the Department of Radiation and Medical Oncology, Zhongnan Hospital of Wuhan University. Thanks for all colleagues' help and guidance.

***Data availability statement*:** The datasets used and/or analysed during the current study available from the corresponding author on reasonable request.

***Ethical approval and consent to participate*:** This study was approved by the medical ethics committee Zhongnan Hospital of Wuhan University [2022019k].

***Conflict of interest statement*:** The authors declare that the research was conducted in the absence of any commercial or financial relationships that could be construed as a potential conflict of interest.

***Funding*:** Technology and Innovation Seed Fund of Zhongnan Hospital, Wuhan University (project number CXPY2023102), Technology and Innovation Seed Fund of Zhongnan Hospital, Wuhan University (project number znpy2019022).

***Authors' contributions*: DJ:** Conception and design of the study; generation of treatment plans; drafting of the article; data analysis; final approval of the version to be published. YT and YP: Conception and design of the study; drafting of the article; data analysis; final approval of the version to be published. LY: Conception and design of the study; drafting of the figures; data analysis. HL: Project design; drafting and final approval of the version to be published. All authors contributed to the article and approved the submitted version.

***AI usage declaration*:** No artificial intelligence (AI) tools were used in the preparation of this manuscript.

REFERENCES

1. Debois M, Oyen R, Maes F, *et al*. (1999) Thecontribution of magnetic resonance imaging to the three-dimensional treatment planning of localized prostate cancer. *Int J Radiat Oncol Biol Phys, **45**: 857-65*.
2. Edmund JM and Nyholm T (2017) A review of substitute CT generation for MRI-only radiation therapy. *Radiation Oncology, **12** (28): 1-15*.
3. Largent A, Barateau A, Nunes J, *et al*. (2019) Pseudo-CT generation for MRI-only radiation therapy treatment planning: comparison among patch-based, atlas-based, and bulk density methods. *Int J Radiat Oncol Biol Phys, **103**(2): 479-490.*
4. Paganelli C, Kipritidis J, Lee D, *et al.* (2018) Image-based retrospective 4D MRI in external beam radiotherapy: A comparative study with a digital phantom. *Medical Physics, **45**(7): 3161-3172*.
5. Farjam R, Tyagi N, Veeraraghavan H, *et al.* (2017) Multiatlas approach with local registration goodness weighting for MRI-based electron density mapping of head and neck anatomy. *Medical Physics, **44**(7): 3706-3717*.
6. Demol B, Boydev C, Korhonen J, *et al.* (2016) Dosimetric characterization of MRI-only treatment planning for brain tumors in atlas-based pseudo-CT images generated from standard T1-weighted MR images. *Medical Physics, **43**(12): 6557*.
7. Brou Boni K, Klein J, Vanquin L, *et al.* (2020) MR to CT synthesis with multicenter data in the pelvic area using a conditional generative adversarial network. *Phys Med Biol, **65**(7): 075002*.
8. Jiang DZ, Dai ZT, Bao ZR *et al.* (2019) CT value organ and homogeneous assigned methods-based radiation treatment planning of pelvic cavity tumors. *International Journal of Radiation Research, **17**(4): 667-674*.
9. Hofmann M, Steinke F, Scheel V, *et al.* (2008) MRI-based attenuation correction for PET/MRI: a novel approach combining pattern recognition and atlas registration. *Journal of Nuclear Medicine, **49**(11): 1875-1883*.
10. Han X (2017) MR-based synthetic CT generation using a deep convolutional neural network method. *Medical Physics, **44**(4): 1408-1419*.
11. Nie D, Trullo R, Lian J, *et al.* (2017) Medical image synthesis with context-aware generative adversarial networks. Medical image computing and computer-assisted intervention; MICCAI.

[DOI: 10.61186/ijrr.24.2.33]

International Conference on Medical Image Computing and Computer-Assisted Intervention, ***10435****: 417-425*.
12. Zhu JY, Park T, Isola P, Efros AA (2017) Unpaired image-to-image translation using cycle-consistent adversarial networks, pp: 2242-2251.
13. Wolterink JM, Dinkla AM, Savenije MHF, *et al.* (2017) Deep MR to CT synthesis using unpaired data. *Simulation and Synthesis in Medical Imaging, p. 14-23*.
14. Liu Y, Lei Y, Wang Y, *et al.* (2019) Evaluation of a deep learning-based pelvic synthetic CT generation technique for MRI-based prostate proton treatment planning. *Phys Med Biol,* ***64****(20): 205022*.
15. Peng Y, Chen S, Qin A, *et al.* (2020) Magnetic resonance-based synthetic computed tomography images generated using generative adversarial networks for nasopharyngeal carcinoma radiotherapy treatment planning. *Radiotherapy and Oncology,* ***150****: 217-224*.
16. Oulbacha R and Kadoury S (2020) MRI to C-arm spine registration through Pseudo-3D CycleGANs with differentiable histograms. *Medical Physics,* ***47****(12): 6319-6333*.
17. Korsholm ME, Waring LW, Edmund JM (2014). A criterion for the reliable use of MRI-only radiotherapy. *Radiat Oncol,* ***9****: 16*.
18. Hsu SH, Han Z, Leeman JE, *et al.* (2022) Synthetic CT generation for MRI-guided adaptive radiotherapy in prostate cancer. *Front Oncol,* ***12****: 969463*.
19. Kang SK, An HJ, Jin H, *et al.* (2021) Synthetic CT generation from weakly paired MR images using cycle-consistent GAN for MR-guided radiotherapy. *Biomed Eng Lett,* ***11****(3): 263-271*.
20. Arabi H, Dowling JA, Burgos N, *et al.* (2018) Comparative study of algorithms for synthetic CT generation from MRI: Consequences for MRI-guided radiation planning in the pelvic region. *Med Phys,* ***45****(11): 5218-5233*.
21. Gholamiankhah F, Mostafapour S, Arabi H (2022) Deep learning-based synthetic CT generation from MR images: comparison of generative adversarial and residual neural networks. *International Journal of Radiation Research,* ***20****(1): 121-130*
22. Henke LE, Contreras JA, Green OL, *et al.* (2018) Magnetic resonance image-guided radiotherapy (MRIgRT): a 4.5-year clinical experience. *Clin Oncol,* ***30****(11): 720-7*.
23. Koivula L, Wee L, Korhonen J (2016). Feasibility of MRI-only treatment planning for proton therapy in brain and prostate cancers: Dose calculation accuracy in substitute CT images. *Med Phys,* ***43****(8): 4634*.
24. Maspero M, van den Berg CAT, Landry G, *et al.* (2017). Feasibility of MR-only proton dose calculations for prostate cancer radiotherapy using a commercial pseudo-CT generation method. *Phys Med Biol,* ***62****(24): 9159-9176*.
25. Hegazy MAA, Cho MH, Cho MH, *et al.* (2019) U-net based metal segmentation on projection domain for metal artifact reduction in dental CT. *Biomed Eng Lett,* ***9****(3): 375-385*.
26. Comelli A, Dahiya N, Stefano A, *et al.* (2020) Deep learning approach for the segmentation of aneurysmal ascending aorta. *Biomed Eng Lett,* ***11****(1): 15-24*.
27. Bourbonne V, Jaouen V, Hognon C, *et al.* (2021) Dosimetric validation of a GAN-based pseudo-CT generation for MRI-only stereotactic brain radiotherapy. *Cancers (Basel),* ***13****(5): 1082*.
28. Lapaeva M, La Greca Saint-Esteven A, Wallimann P, *et al.* (2025) A comprehensive comparative study of generative adversarial network architectures for synthetic computed tomography generation in the abdomen. *Med Phys,* ***52****(8): e18038*.
29. Thwaites D (2013). Accuracy required and achievable in radiotherapy dosimetry: have modern technology and techniques changed our views? *Journal of Physics Conference,* ***444****: 012006*.
30. Wyatt JJ, Pearson RA, Walker CP, *et al.* (2021). Cone beam computed tomography for dose calculation quality assurance for magnetic resonance-only radiotherapy. *Phys Imaging Radiat Oncol,* ***17****: 71-76*.

[DOI: 10.61186/ijrr.24.2.33]